Structure and Catalytic Behavior of Alumina Supported Bimetallic Au-Rh Nanoparticles in the Reduction of NO by CO

Xianwei Wang [1], Hongji Wang [1], Nobutaka Maeda [1,*] and Alfons Baiker [2,*]

[1] Key Laboratory of Industrial Ecology and Environmental Engineering, School of Environmental Science and Technology, Dalian University of Technology, Dalian 116024, China; xianwei.wang@unige.ch (X.W.); wanghongji419@163.com (H.W.)

[2] Department of Chemistry and Applied Biosciences, Institute for Chemical and Bioengineering, ETH Zurich, Hönggerberg, HCI, CH-8093 Zurich, Switzerland

[*] Correspondence: nobutaka.maeda@dlut.edu.cn (N.M.); alfons.baiker@chem.ethz.ch (A.B.);
Tel.: +81-090-6742-4738 (N.M.); +41-44-632-3153 (A.B.)

Abstract: Alumina-supported bimetallic AuRh catalysts, as well as monometallic reference catalysts, were examined with regard to their structural and catalytic properties in the reduction of NO by CO. Depending on the molar ratio of Au:Rh, the nanoparticles prepared by borohydride co-reduction of corresponding metal salt solutions had a size of 3.5–6.7 nm. The particles consisted of well-dispersed noble metal atoms with some enrichment of Rh in their surface region. NO conversion of $AuRh/Al_2O_3$ shifted to lower temperatures with increasing Rh content, reaching highest activity and highest N_2 selectivity for the monometallic Rh/Al_2O_3 catalyst. This behavior is attributed to the enhanced adsorption of CO on the bimetallic catalyst resulting in unfavorable cationic Rh clusters Rh^+-$(CO)_2$. Doping with ceria of $AuRh/Al_2O_3$ and Rh/Al_2O_3 catalysts increased the surface population of metallic Rh sites, which are considered most active for the reduction of NO by CO and enhancement of the formation of intermediate isocyanate (-NCO) surface species and their reaction with NO to form N_2 and CO_2.

Keywords: alumina-supported AuRh nanoparticles; ceria doping; in situ DRIFTS; nitric oxide reduction with carbon monoxide; reaction mechanism

1. Introduction

Anthropogenic emissions of nitrogen oxides from fuel combustion processes pose a serious threat to human health. Since the reaction of CO and NO can eliminate two harmful pollution gases simultaneously, it has attracted a great deal of attention especially in automobile exhaust applications in a wide range of temperature and pressure [1,2]. Typically, noble metals such as Rh, Pt, and Pd are employed for the NO reduction and CO oxidation [3–9]. Among the studies reported so far, the NO reduction by CO and co-adsorption on Pd surfaces, as well as co-adsorption of NO and CO on platinum catalysts, have been extensively studied [6–9]. The formation and migration of isocyanate species are considered to be crucial for efficient catalytic cycles [8].

Due to its low reactivity, gold has long been disregarded as a candidate for heterogeneous catalysis until its nanoparticles supported on oxidic materials were discovered to catalyze the oxidation of CO even below room temperature [10]. The choice of metal oxide supports strongly affects the structural and chemical properties of Au–metal oxide interfaces and is therefore a crucial factor in the design of such catalysts [11–16]. The unique properties of gold, such as chemical

stability, non-toxicity, and biocompatibility [11], make gold catalysts attractive for various reactions, including oxidations and hydrogenations [17–20]. Gold and its alloys with other metals show interesting performance in the NO reduction by CO, and thus, structurally optimized Au catalysts provide an attractive research direction [16]. Different Au-based catalysts synthesized by coprecipitation or deposition–precipitation methods have been tested for this reaction [15,21–24], among which Au supported on Fe-loaded ceria shows high NO conversion and stability [21]. Au–Pd alloy catalysts exhibit high selectivity, compared to pure Pd catalysts [25], showing further potential of bimetallic gold-based catalysts.

Generally, the reaction steps of NO reduction by CO can be expressed as follows [7,26]:

$$2CO + 2NO \rightarrow N_2 + 2CO_2, \tag{1}$$

$$CO + 2NO \rightarrow N_2O + CO_2, \tag{2}$$

$$CO + N_2O \rightarrow N_2 + CO_2. \tag{3}$$

Reaction (1) directly forms N_2 while an alternative path requires reactions (2) and (3), where N_2O is formed as an intermediate. Depending on the metal oxide support, Au nanoparticles offer high N_2 selectivity, whereas the main product is N_2O over unsupported Au catalysts [22,25]. Therefore, the presence of pertinent Au–metal oxide interfaces promotes reactions (1) and (3). In situ IR spectroscopic studies revealed that CO and NO adsorb in various configurations, i.e., on-top $Au^{\delta+}$-CO, CO on Au^0 particles (Au_s^0-CO), bridged NO (Au-NO), and on-top NO^- species (Au-NO^-) [23,27–29]. Their reaction on the Au surface forms isocyanate (-NCO) species, which are considered to be a key reaction intermediate that migrates to the oxide support [30,31].

In recent research on NO_x reduction, ceria as a support material or as a promoter of the active metals has been the focus for activity enhancement [32,33]. Different dispersions and sizes of CeO_2 nanoparticles influence the catalytic performance [34]. The use of ceria was reported to induce strong metal–support interaction (SMSI) with active metal components. The dispersion of the metal was thus improved by the SMSI effect [32,35,36]. Besides, the oxygen vacancies, present at the interface between the ceria and the metal, impart high oxygen storage capacity to the catalyst and facilitate the transport of oxygen from the ceria to the metal surface, resulting in high activity for NO_x reduction [37–39].

Bimetallic gold-based alloys can offer interesting synergistic effects in catalysis [40]. While the reduction of NO by CO on bimetallic gold-based alloy catalysts containing Pt and Pd has been the focus of various studies [41–44], there exist only a few reports in the literature where the behavior of bimetallic AuRh catalysts has been investigated [45–49]. This may be attributed to the large miscibility gap of the AuRh system [50]. However, it has been shown that borohydride co-reduction of metal salt solutions yields nanoparticles in the bulk-immiscible AuRh system [47,51]. To the best of our knowledge, there exists no report where supported bimetallic AuRh catalysts have been examined for the reduction of NO by CO. Its alloying with Au could result in a favorable catalytic synergy effect, as it has been observed in other reactions [49,51]. With this in mind, we have investigated the structural and chemical properties of pure and ceria-promoted alumina-supported bimetallic AuRh alloy nanoparticles and examined their potential for the catalytic reduction of NO by CO.

2. Results and Discussion

2.1. Bimetallic AuRh/Al₂O₃ Catalysts

2.1.1. Catalyst Characterization

XRD patterns of the catalysts are shown in Figure 1. The diffraction patterns at 38.1°, 44.3°, 64.6°, and 77.6°, assigned to Au(111), Au(200), Au(220), and Au(311), respectively, were clearly observed for Au/Al₂O₃ and AuRh(3:1)/Al₂O₃ catalysts (molar ratios of Au:Rh in the catalysts are given in parentheses) [52]. Further addition of Rh caused a considerable broadening of the Au(111) reflection

and a slight shift toward the Rh(111) reflection ($2\theta = 41.0°$) [53,54]. There were no distinct diffraction peaks of Au and Rh observed for AuRh(1:1)/Al$_2$O$_3$ and AuRh(1:3)/Al$_2$O$_3$ catalysts, implying that these catalysts consisted predominantly of well-dispersed bimetallic AuRh nanoparticles on Al$_2$O$_3$ [54].
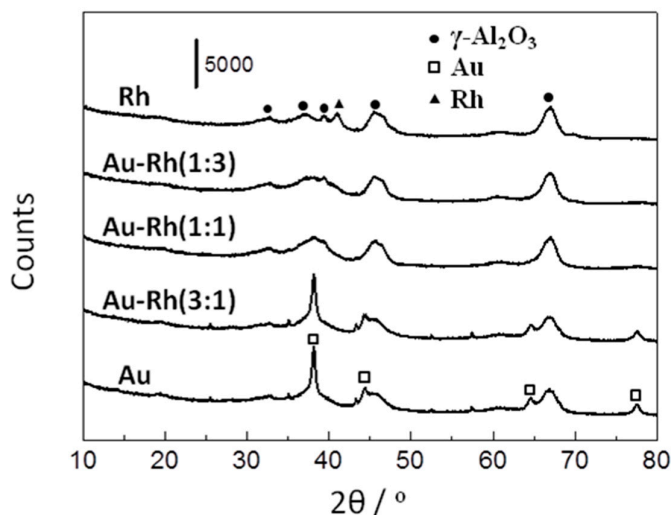

Figure 1. XRD patterns of Au/Al$_2$O$_3$, Rh/Al$_2$O$_3$, and AuRh/Al$_2$O$_3$ catalysts with specified molar ratios of Au:Rh.

Figure 2 shows STEM images and metal particle size distributions of various catalysts. Monometallic Au particles in the Au/Al$_2$O$_3$ catalyst were relatively large, whereas their alloying with Rh resulted in well-dispersed small nanoparticles on the Al$_2$O$_3$ surface. EDX line scans of selected bimetallic particles, displayed in Figure 3, showed that Au and Rh atoms were almost uniformly present in the bimetallic nanoparticles. The apparent absence of bimetallic particles with a distinct core/shell structure, e.g., that often observed for bimetallic PdAu particles [55], might be attributed to the high inter-diffusion rate of Rh and Au atoms in the bimetallic particles [56,57] and the fact that the catalysts were pretreated in H$_2$ at 300 °C before characterization [55].
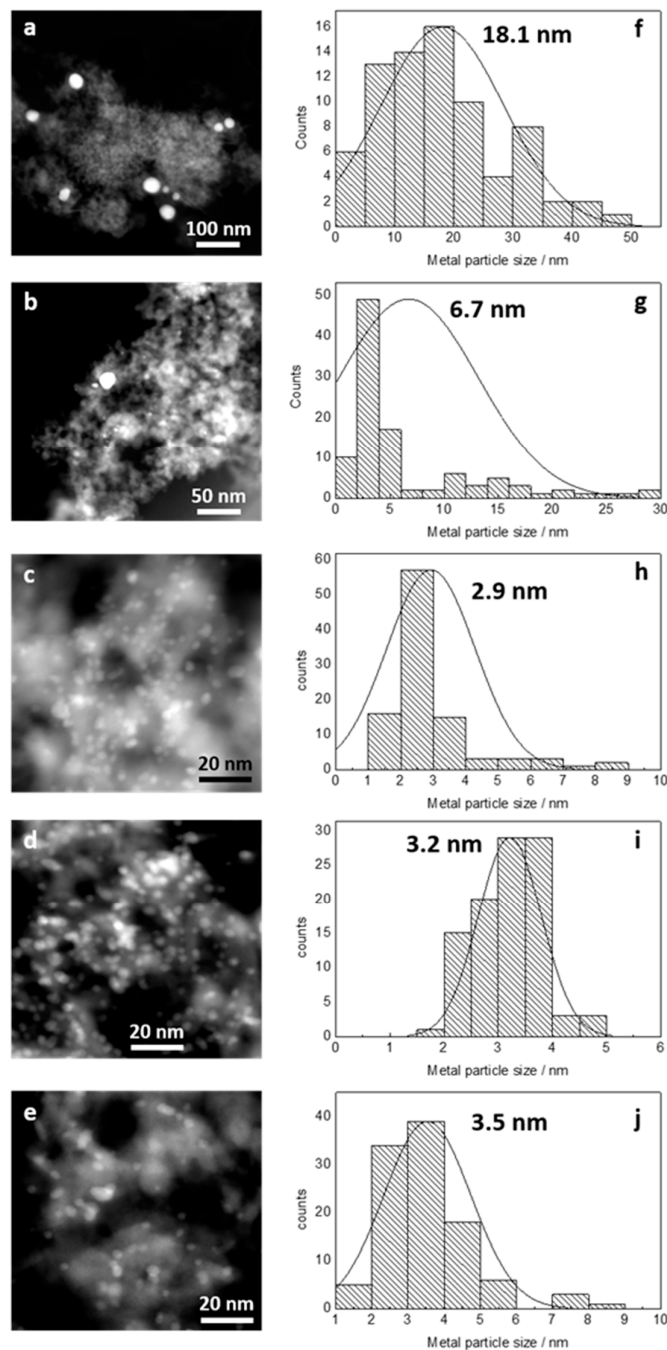
Figure 2. Scanning transmission electron microscopy (STEM) images of different catalysts: (**a**) Au/Al$_2$O$_3$, (**b**) AuRh(3:1)/Al$_2$O$_3$, (**c**) AuRh(1:1)/Al$_2$O$_3$, (**d**) AuRh(1:3)/Al$_2$O$_3$, and (**e**) Rh/Al$_2$O$_3$ catalysts. Particle size distributions of different catalysts: (**f**) Au/Al$_2$O$_3$, (**g**) AuRh(3:1)/Al$_2$O$_3$, (**h**) AuRh(1:1)/Al$_2$O$_3$, (**i**) AuRh(1:3)/Al$_2$O$_3$, and (**j**) Rh/Al$_2$O$_3$ catalysts. The average particle sizes of the catalysts are indicated in the histograms.
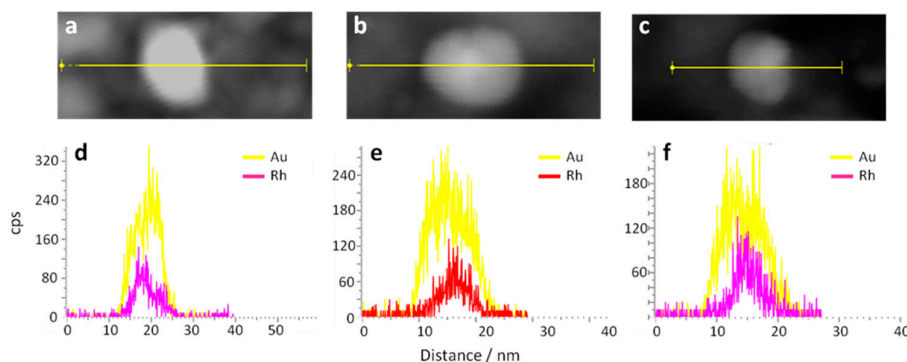
Figure 3. STEM images of selected bimetallic particles: (**a**) AuRh(3:1)/Al₂O₃, (**b**) AuRh(1:1)/Al₂O₃, and (**c**) AuRh(1:3)/Al₂O₃. Energy-dispersive X-ray spectroscopy (EDX) line scans of selected bimetallic particles: (**d**) AuRh(3:1)/Al₂O₃, (**e**) AuRh(1:1)/Al₂O₃, and (**f**) AuRh(1:3)/Al₂O₃.

Table 1 summarizes the results of XPS analyses of the catalysts pretreated with pure H_2 (100 mL/min) at 300 °C for 1 h. The raw XPS spectra without background subtraction are shown in Figure S1 (Supplementary Materials). The Au $4f_{7/2}$ photoelectron peak at a binding energy (BE) between 83.7 and 83.9 eV is attributed to the metallic Au^0 species. The reason for the slight shifts of the Au $4f_{7/2}$ (84 eV) and Rh $3d_{5/2}$ (307.6) signals is probably due to cluster size effects [58] or charging of the samples that mainly consisted of nonconductive Al₂O₃. As shown in Table 1, the atomic ratios of Au/(Au+Rh) were lower than those expected from the nominal bulk composition of the catalysts, indicating the presence of a segregated Rh-enriched phase in the near-surface region probably due to pretreatment with hydrogen.

Table 1. BET, STEM and X-ray photoelectron spectroscopy (XPS) analyses of Au/Al₂O₃, Rh/Al₂O₃, and AuRh/Al₂O₃ catalysts with specified molar ratios of Au:Rh.

Catalyst	BET surface area (m²/g)	Mean Size of metal Particles (nm)	XPS		
			Binding energy of Au4f$_{7/2}$ (eV)	Binding energy of Rh3d$_{5/2}$ (eV)	$\frac{Au}{Au + Rh}$
Rh/Al₂O₃	160	3.5	-	307.3	0
Au-Rh(1:3)/Al₂O₃	154	3.2	83.7	307.1	0.24
Au-Rh(1:1)/Al₂O₃	163	2.9	83.7	307.0	0.43
Au-Rh(3:1)/Al₂O₃	161	6.7	83.9	306.9	0.63
Au/Al₂O₃	171	18.1	83.9	-	1.00

2.1.2. Catalytic Performance

The behavior (NO conversion and N_2 selectivity) of the AuRh/Al₂O₃ catalysts with different compositions is shown in Figure 4. The Au/Al₂O₃ catalyst showed poor performance and no N_2 selectivity even at 250 °C. This is partly attributed to the relatively large size of the deposited gold

particles and poor activity for the reduction of the formed N_2O by CO (reaction (3)). The higher the Rh content was, the better the activity was, while the N_2 selectivity was zero for temperatures up to 200 °C with all bimetallic catalysts (see also Table S1 in Supplementary Materials). The increase in the N_2 selectivity by the Rh addition is attributed to an increase of the rate of reaction (3). The only by-product was N_2O, while NO_2 was not detected. Note that Rh/Al_2O_3 outperformed all bimetallic AuRh catalysts. To gain some insight into the role of both metals, Au and Rh, in the NO reduction by CO, we used the in situ DRIFT spectroscopy.
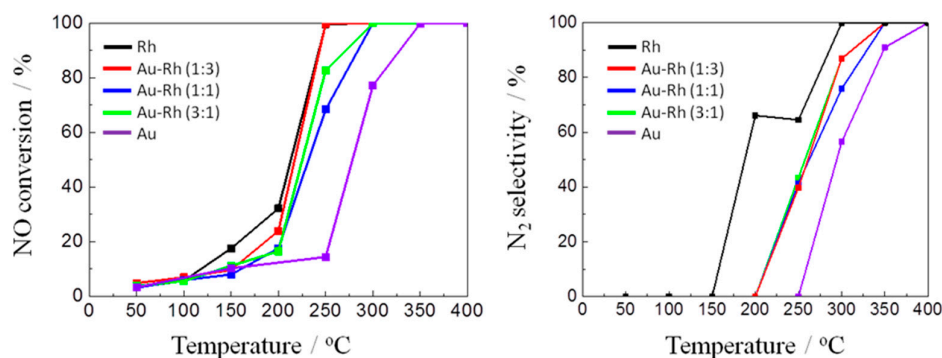

Figure 4. NO conversion and N_2 selectivity of Au/Al_2O_3, Rh/Al_2O_3, and $AuRh/Al_2O_3$ catalysts with different molar ratios of Au:Rh. Conditions: gas mixture, 2000 ppm NO, 2000 ppm CO, and He balance; total flow rate, 150 mL/min; gas hourly space velocity (GHSV), 18,000 h^{-1}; reaction temperature: 50–400 °C.

2.1.3. In Situ DRIFTS Study

In situ DRIFTS spectra taken during the adsorption of 2000 ppm CO in He balance at 30 °C for 5 min (from the red line to the blue line at an interval of 1 min) are shown in Figure 5. The adsorption temperature was set to 30 °C to suppress disturbing desorption and disproportionation of CO and NO. At the initial stage of CO adsorption, a sharp band at 2069 cm^{-1} assignable to on-top CO on metallic Rh (Rh^0-CO) emerged [59], followed by a gradual increase in bridged CO (1910 cm^{-1}) [60,61] together with twin bands at 2091 cm^{-1} and 2025 cm^{-1}, which were assigned to asymmetric and symmetric stretching vibrations of gem-dicarbonyls on Rh cations, Rh^+-$(CO)_2$ [60]. As evident from the XPS data, the Rh particles existed as metallic Rh after H_2 pretreatment. However, CO adsorption caused the decomposition of the Rh particles by dispersing cationic Rh atoms as Rh^+-$(CO)_2$ [62,63]. Interestingly, by adding Au, the intensity of these bands increased and reached a maximum for the $AuRh(1:1)/Al_2O_3$ catalyst. A similar tendency was also observed for on-top CO, indicating that the presence of Au promoted the CO adsorption on the Rh sites. Further addition of Au, as realized in the $AuRh(3:1)/Al_2O_3$ catalyst, decreased the intensity by a factor of ca. 10, and the Au/Al_2O_3 catalyst showed only weak bands at 2102 cm^{-1} and 2170 cm^{-1}, which were assigned to CO adsorbed on Au and Al_2O_3, respectively [64]. Remarkably, the addition of Au induced the formation of Rh^+-$(CO)_2$ species, which are considered to be dispersed in the form of small clusters [60]. This phenomenon is in good agreement with the XRD data (Figure 1), showing that the diffraction peaks were broadened by alloying Rh with Au.
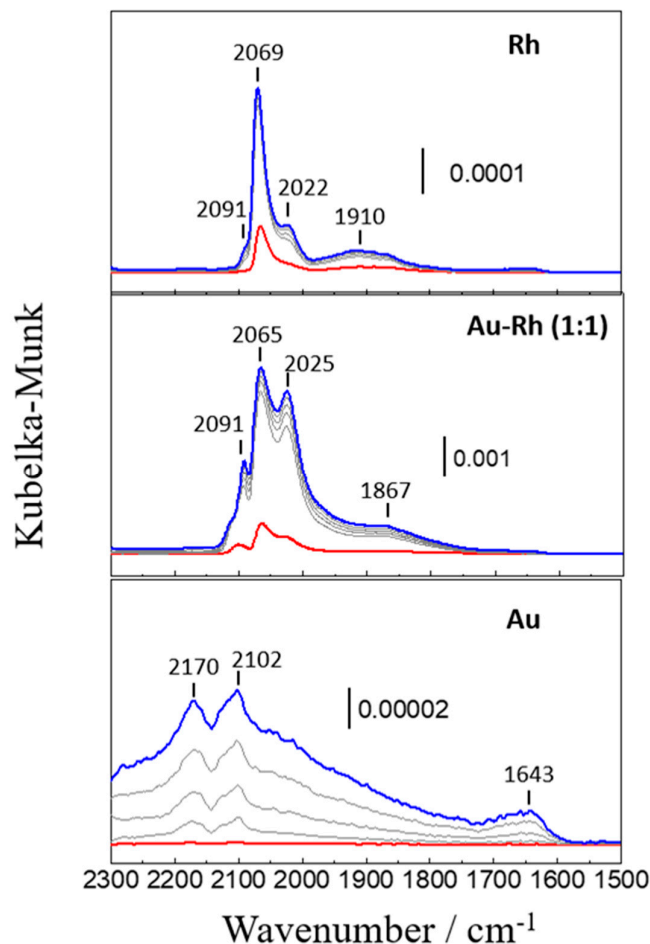
Figure 5. In situ diffuse reflectance IR spectroscopy (DRIFTS) spectra recorded during CO adsorption on the Rh/Al_2O_3, $AuRh(1:1)/Al_2O_3$, and Au/Al_2O_3 catalysts at 30 °C for 5 min (from the red line to the blue line at an interval of 1 min). Gas mixture: 2000 ppm CO and He balance; total flow rate: 100 mL/min.

DRIFTS spectra measured during NO adsorption (gas mixture: 2000 ppm NO in He balance, total flow rate: 100 mL/min, temperature: 30 °C, and time duration: 5 min) are shown in Figure 6. A sharp band at 1684 cm^{-1} and a weak band at 1801 cm^{-1}, which can be assigned to on-top NO$^{\delta-}$ and on-top NO, respectively, were observed for the Rh/Al_2O_3 catalyst [3,65]. Bridged NO was not observed in our study. The presence of gold promoted the adsorption of NO, especially for Rh-NO at ca. 1800 cm^{-1} but decreased the ratio of Rh-NO$^{\delta-}$. This was induced by the low electron density of cationic Rh (Rh$^+$) for AuRh alloy nanoparticles as evident from the CO adsorption in Figure 5. Therefore, the formation of cationic Rh suppressed the electron back-donation to NO molecules, which did not allow for the negatively-charged on-top NO$^{\delta-}$ configuration. For the Au/Al_2O_3 catalyst, a broad band at 1652 cm^{-1} assigned to $_{asym}(NO_2)$ of surface NO_2 species was observed [23]. The band at 1540 cm^{-1} is attributed to bridging nitrito (NO_2^-) in the chelated state [66]. An additional band at 1894 cm^{-1} was assigned to NO adsorbed on Au [67]. Co-adsorption of NO and CO indicated that NO was adsorbed on Rh more strongly than CO (DRIFTS spectra are provided in Figure S2 in Supplementary Materials). However, the AuRh alloy catalysts tended to enrich CO on the surface. This might be the reason why the conversion decreased for the AuRh alloy catalysts due to high CO coverage suppressing the NO adsorption and dissociation.
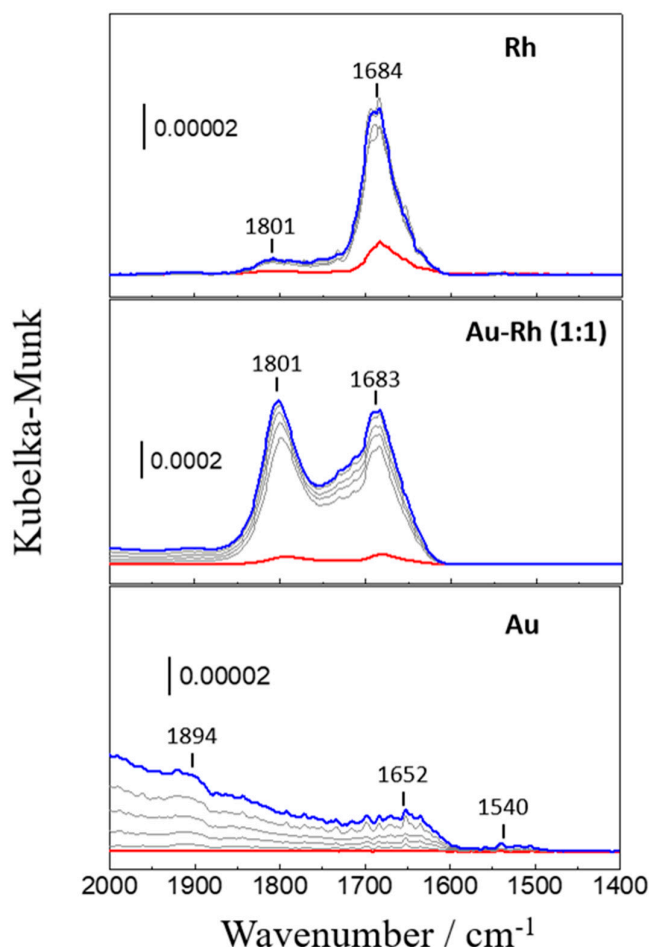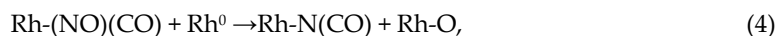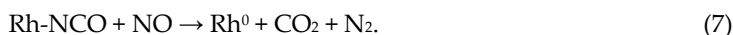
Figure 6. In situ DRIFTS spectra recorded during NO adsorption on Rh/Al_2O_3, $AuRh(1:1)/Al_2O_3$, and Au/Al_2O_3 catalysts at 30 °C for 5 min (from the red line to the blue line at an interval of 1 min). Gas mixture: 2000 ppm NO and He balance; total flow rate: 100 mL/min.

Figure 7 shows DRIFTS spectra during the reduction of NO by CO at 300 °C for 10 min (from the red line (5 s) to the blue line (10 min) at an interval of 1 min; the green line represents a spectrum after 1 min of reaction). At this high temperature, desorption and reaction of NO and CO took place rapidly and the corresponding bands were greatly weakened. Instead, several new bands appeared, which are centered at 2254 cm^{-1}, 1634 cm^{-1}, and 1404 cm^{-1}, respectively. The catalyst surface was dominated by isocyanate species (-NCO) detected at 2254 cm^{-1}. The blue shift compared to previous reports results from the presence of Rh^+ sites [4]. The shoulder band at ca. 2230 cm^{-1} was assigned to Rh^0-NCO, which completely disappeared for the $AuRh(3:1)/Al_2O_3$ catalyst. Because N_2O was not detected in the gas phase, the contribution of IR bands of gaseous N_2O in this region can be excluded. The intensity of isocyanate species first increased, reached a maximum after 4 min (green line), and then diminished (blue line), accompanied by a weak band at 2049 cm^{-1} assigned to carbonyl species adsorbed on Rh [3,4]. By adding Au, the intensity of isocyanate species increased and their decomposition also occurred rather rapidly. The decomposition process is better highlighted by switching the gaseous compositions to only 2000 ppm NO in He balance (Figure S3 in Supplementary Materials).

A plausible reaction pathway is shown as follows:

$$Rh\text{-}(NO)(CO) + Rh^0 \rightarrow Rh\text{-}N(CO) + Rh\text{-}O, \qquad (4)$$

$$Rh\text{-}N(CO) \rightarrow Rh\text{-}NCO, \qquad (5)$$

$$Rh\text{-}O + CO \rightarrow Rh^0 + CO_2, \tag{6}$$

$$Rh\text{-}NCO + NO \rightarrow Rh^0 + CO_2 + N_2. \tag{7}$$

A sharp band at 1404 cm^{-1} was assigned to nitrate species bonding to both Rh and oxidic support [4], which diminished by adding Au. The negatively charged Rh-(NO)$^{\delta-}$ at 1680 cm^{-1} and 1634 cm^{-1} is considered as an active precursor for a key surface reaction step during NO–CO reaction [68,69]. The lowered wavenumber of Rh-NO$^{\delta-}$ indicates a weakening of the N–O bond and strengthening of the Rh–N bond due to electron back-donation to the N–O antibonding orbital [68,69], resulting in higher propensity of NO molecules to be dissociated over reduced Rh surfaces to yield nitride and adsorbed oxygen atoms:
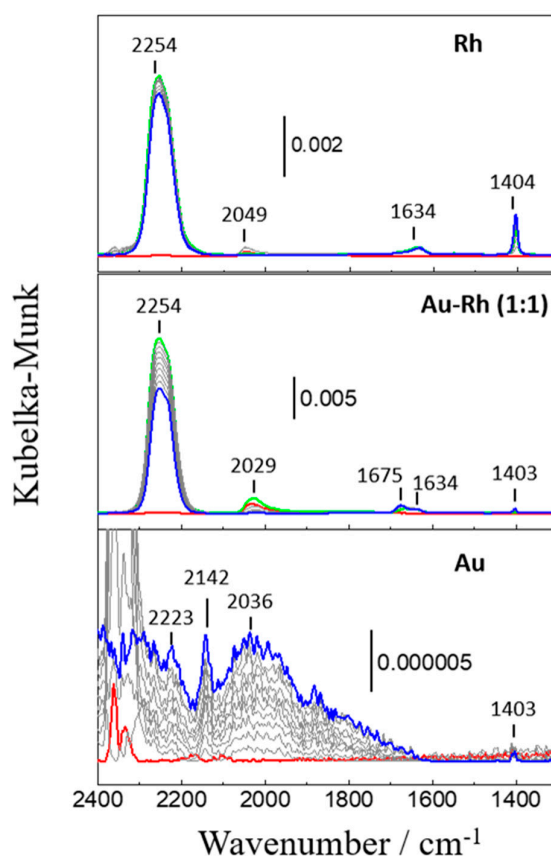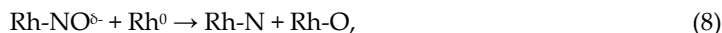
$$Rh\text{-}NO^{\delta-} + Rh^0 \rightarrow Rh\text{-}N + Rh\text{-}O, \tag{8}$$

$$Rh\text{-}N + Rh\text{-}NO \rightarrow Rh\text{-}N_2O. \tag{9}$$

Figure 7. In situ DRIFTS spectra recorded during NO–CO reaction on the Rh/Al$_2$O$_3$, AuRh(1:1)/Al$_2$O$_3$, and Au/Al$_2$O$_3$ catalysts at 300 °C for 10 min (from the red line to the blue line at an interval of 1 min). Gas mixture: 2000 ppm NO, 2000 ppm CO, and He balance; total flow rate: 100 mL/min.

2.2. Effects of CeO$_2$ Addition

2.2.1. Catalyst Characterization

From reactions (4)–(9) described above, it is obvious that redox reactions play a key role in the reduction of NO by CO, as indicated by the oxidation of Rh by NO dissociation and the reduction of Rh-O by CO. Cerium oxides are well known to facilitate redox processes by transformation between Ce$_2$O$_3$ and CeO$_2$ [37–39]. With this in mind, we impregnated ceria onto the best performing binary

catalyst, AuRh(1:1)/Al$_2$O$_3$ catalyst. The resulting catalyst was designated henceforth as AuRh–CeO$_x$/Al$_2$O$_3$ and had a AuRh:Ce molar ratio of 1:1.

Properties of the AuRh–CeO$_x$/Al$_2$O$_3$ catalyst and the corresponding reference catalysts with similar amounts of Ce, Au–CeO$_x$/Al$_2$O$_3$ and Rh–CeO$_x$/Al$_2$O$_3$, are summarized in Table 2. The surface areas of the three ceria-promoted catalysts slightly decreased compared to those of the corresponding nonpromoted samples (Table 1).

Table 2. BET, STEM, and XPS analyses of Au–CeO$_x$/Al$_2$O$_3$, AuRh–CeO$_x$/Al$_2$O$_3$, Rh–CeO$_x$/Al$_2$O$_3$, and CeO$_x$/Al$_2$O$_3$ catalysts with different molar ratios of AuRh:Ce.

Catalyst	BET surface area (m^2/g)	Mean Size of AuRh Particles (nm)	XPS			
			Binding energy of Au4f$_{7/2}$ (eV)	Binding energy of Rh3d$_{5/2}$ (eV)	Au / Au + Rh	Ce^{3+} / Ce^{3+} + Ce^{4+}
Au-Ce/Al$_2$O$_3$	132	5.7	83.9	-	-	0.34
AuRh-Ce/Al$_2$O$_3$	154	3.1	84.0	307.3	0.37	0.56
Rh-Ce/Al$_2$O$_3$	107	3.8	-	307.5	-	0.42

XRD analyses (Figure 8) indicated that the addition of ceria induced the formation of crystalline gold domains in the bimetallic AuRh particles, as evident from the emergence of Au(111), Au(200), Au(220), and Au(311) reflections. In contrast, the intensity of diffraction patterns due to crystalline Rh stayed extremely weak and broad, indicating that the Rh nanoparticles were still well-dispersed on the surface. Reflections due to crystalline CeO$_2$ were not discernible for AuRh–CeO$_x$/Al$_2$O$_3$, suggesting the formation of amorphous ceria dispersed on the surface. Figure 9 shows STEM images and particle size distributions of the AuRh–CeO$_x$/Al$_2$O$_3$ catalyst and the reference catalysts. The addition of CeO$_x$ had little influence on the size of the bimetallic AuRh particles (3.1 nm shown in Table 2), whereas it was significant for the Au–CeO$_x$/Al$_2$O$_3$ and Rh–CeO$_x$/Al$_2$O$_3$ catalysts.

Table 2 also summarizes results of XPS analyses of Au 4f, Rh 3d, and Ce 3d. The corresponding raw XPS spectra are provided in Supplementary Materials (Figure S4). A mixture of Ce^{3+} and Ce^{4+} oxidation states existed on the surface of the catalysts [70,71]. Hereafter, the cerium oxides are denoted as CeO$_x$ ($x = 1.5$–2). As shown in Table 2, the concentration of Ce^{3+} in the AuRh–CeO$_x$/Al$_2$O$_3$ catalyst is higher than those of the monometallic reference catalysts and CeO$_x$/Al$_2$O$_3$ catalyst, indicating that the presence of bimetallic AuRh promotes the formation of Ce^{3+} components as Ce$_2$O$_3$.

H$_2$ TPR profiles (Figure S5 in Supplementary Materials) revealed that the presence of bimetallic AuRh particles lowered the reduction temperature of CeO$_x$ components from 400 to less than 200 °C.
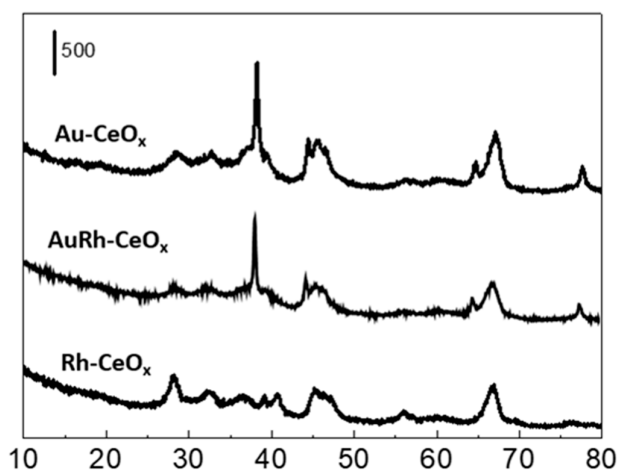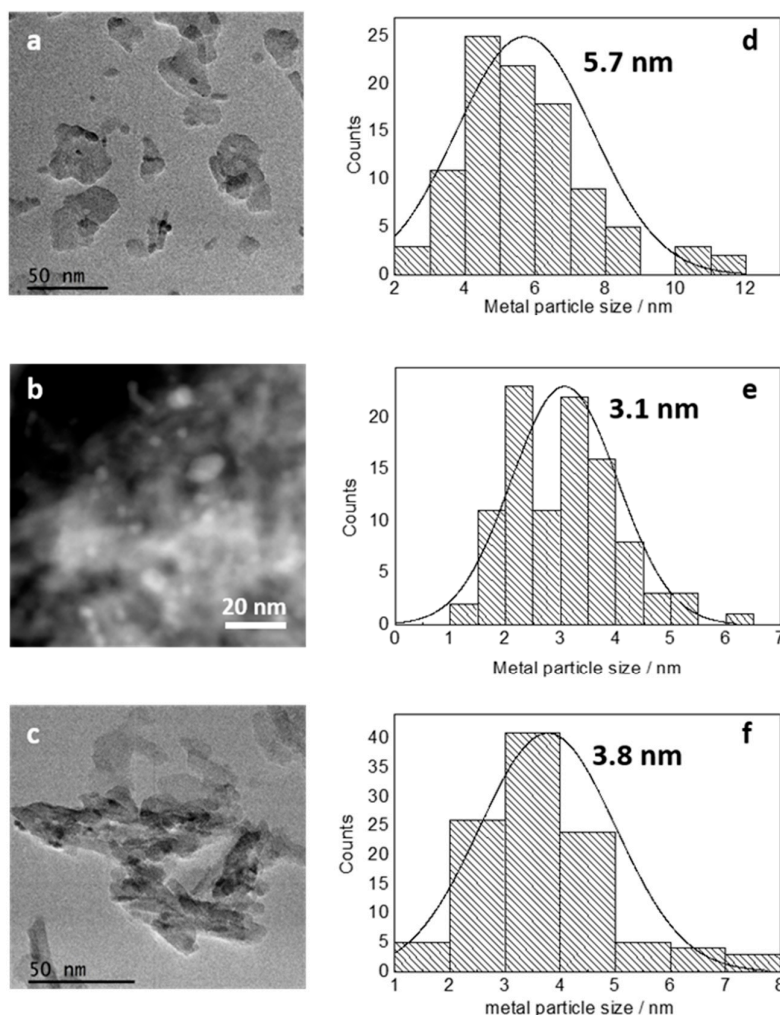
Figure 9. STEM images of different catalysts: (**a**) Au–Ce/Al$_2$O$_3$, (**b**) AuRh–CeO$_x$/Al$_2$O$_3$, and (**c**) Rh–Ce/Al$_2$O$_3$. Particle size distributions of different catalysts: (**d**) Au–Ce/Al$_2$O$_3$, (**e**) AuRh–CeO$_x$/Al$_2$O$_3$, and (**f**) Rh–Ce/Al$_2$O$_3$. The average particle sizes are indicated in the histograms.

2.2.2. Catalytic Performance

Figure 10 shows the NO conversion and N$_2$ selectivity achieved in the reduction of NO by CO for the AuRh–CeO$_x$/Al$_2$O$_3$ catalyst and the reference catalysts Au/CeO$_x$/Al$_2$O$_3$ and Rh/CeO$_x$/Al$_2$O$_3$. The comparison with the corresponding catalysts without ceria addition (Figure 4) showed that ceria doping enhances the catalytic performance of AuRh/Al$_2$O$_3$ and Rh/Al$_2$O$_3$ catalysts, whereas that of the Au/Al$_2$O$_3$ catalyst declines. Both NO conversion and N$_2$ selectivity curves of the AuRh/Al$_2$O$_3$ and Rh/Al$_2$O$_3$ catalysts are shifted towards lower temperature. In contrast, the catalytic performance declined with CeO$_x$ deposition on the Au/Al$_2$O$_3$ catalyst. The N$_2$ selectivity of AuRh/Al$_2$O$_3$ catalyst was zero at temperatures up to 200 °C but increased to 69% for the corresponding ceria-promoted AuRh–CeO$_x$/Al$_2$O$_3$ catalyst, as shown in Table S2 (Supplementary Materials). The only by-product was N$_2$O. This implied that the addition of CeO$_x$ facilitated the reduction of N$_2$O by CO, i.e., reaction (3) described in the Introduction section. Note that the N$_2$ selectivity of the AuRh)/Al$_2$O$_3$ catalyst showed some fluctuation, depending on the reaction temperature. Since this behavior was perfectly reproducible, we supposed that it is due to a chemical or structural change of the catalysts, possibly

leading to a mechanistic change of which clarification needs further investigations. Note that such behavior has earlier been observed in some cases for metal alloys [72] and metal–metal oxide nanocomposites [73,74].
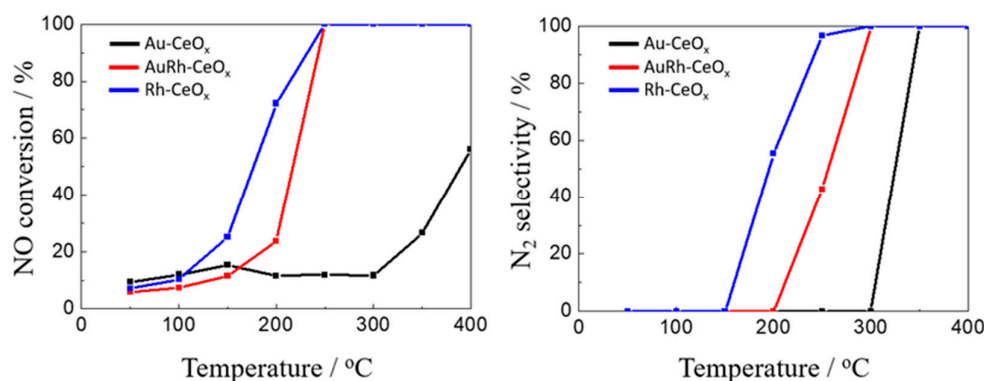

Figure 10. NO conversion and N_2 selectivity of the Au–CeO$_x$/Al$_2$O$_3$ AuRh–CeO$_x$/Al$_2$O$_3$, and Rh–CeO$_x$/Al$_2$O$_3$ catalysts. Conditions: gas mixture, 2000 ppm NO, 2000 ppm CO, and He balance; total flow rate, 150 mL/min; GHSV, 18,000 h^{-1}; temperature range, 50–450 °C.

2.2.3. In Situ DRIFTS Study

To unveil the role of CeO$_x$ in the reduction of NO by CO, in situ DRIFTS studies were carried out. Figure 11 shows DRIFT spectra measured during the adsorption of 2000 ppm CO in He balance at 30 °C for 5 min (from the red line to the blue line at an interval of 1 min). By the addition of CeO$_x$, the intensity of the band of on-top CO at 2065 cm^{-1} became dominant while the bands of Rh$^+$-(CO)$_2$ at 2091 cm^{-1} and 2025 cm^{-1} were considerably weakened, indicating that there are less Rh$^+$ sites in the presence of CeO$_x$. This alludes that Rh$^+$ sites are less active for the reaction and the presence of CeO$_x$ enhances the formation of Rh^0 sites, which facilitate the reduction of NO by CO. However, larger amounts of CeO$_x$ addition resulted in a dramatic decrease in the intensity of adsorbed CO due to higher coverage of CeO$_x$ on the bimetallic AuRh particles.
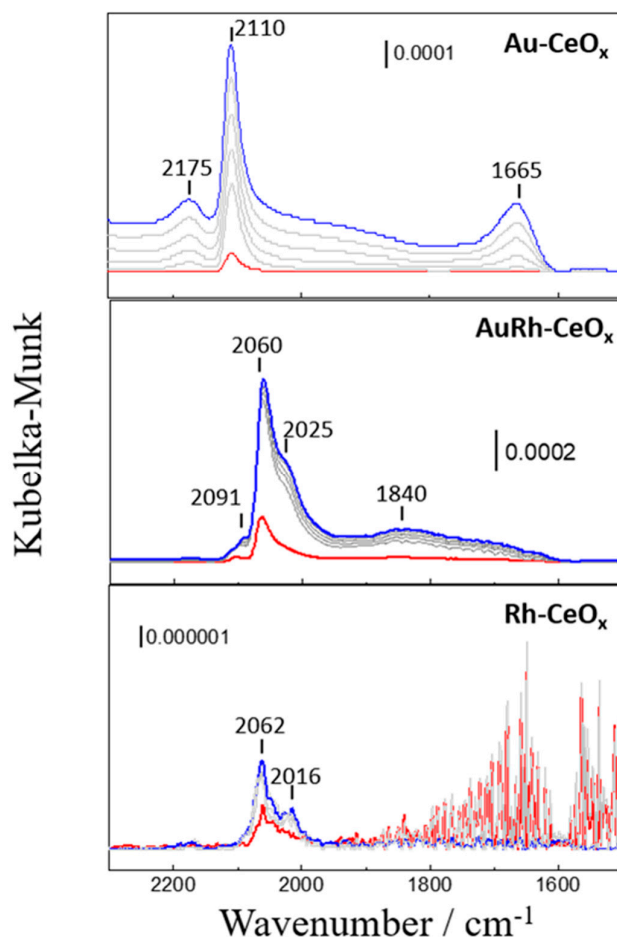
Figure 11. In situ DRIFTS spectra recorded during CO adsorption on the Au–CeO$_x$/Al$_2$O$_3$, AuRh–CeO$_x$/Al$_2$O$_3$, and Rh–CeO$_x$/Al$_2$O$_3$ at 30 °C for 5 min (from the red line to the blue line at an interval of 1 min). Gas mixture: 2000 ppm CO and He balance; total flow rate: 100 mL/min.

DRIFT spectra of NO adsorptions are displayed in Figure 12. In line with the CO adsorption, the band at a higher wavenumber (ca. 1800 cm^{-1}) was weakened by the CeO$_x$ addition. The relative increase in the band at 1683 cm^{-1} indicated that the CeO$_x$ promoted the transformation of the adsorption configuration from Rh-NO to Rh-NO$^{\delta-}$. As described in Section 2.1.3, the enriched on-top NO$^{\delta-}$ is indicative of the formation of metallic Rh and the strong electron back-donation from Rh to anti-bonding orbitals of adsorbed NO molecules. The rate constants for NO dissociation determines the activity of the catalysts [68]. Therefore, the dissociation of the negatively charged NO on metallic Rh is a key step for the reduction of NO with CO. A new band at 1890 cm^{-1} for catalysts promoted with ceria is assigned to adsorbed NO as Au^{n+}-NO ($n \approx 0$) complex [68]. DRIFT spectra during co-adsorption of NO and CO demonstrated that CO molecules were adsorbed mainly on cationic Rh while NO molecules occupied metallic Rh (Figure S6 in Supplementary Materials).
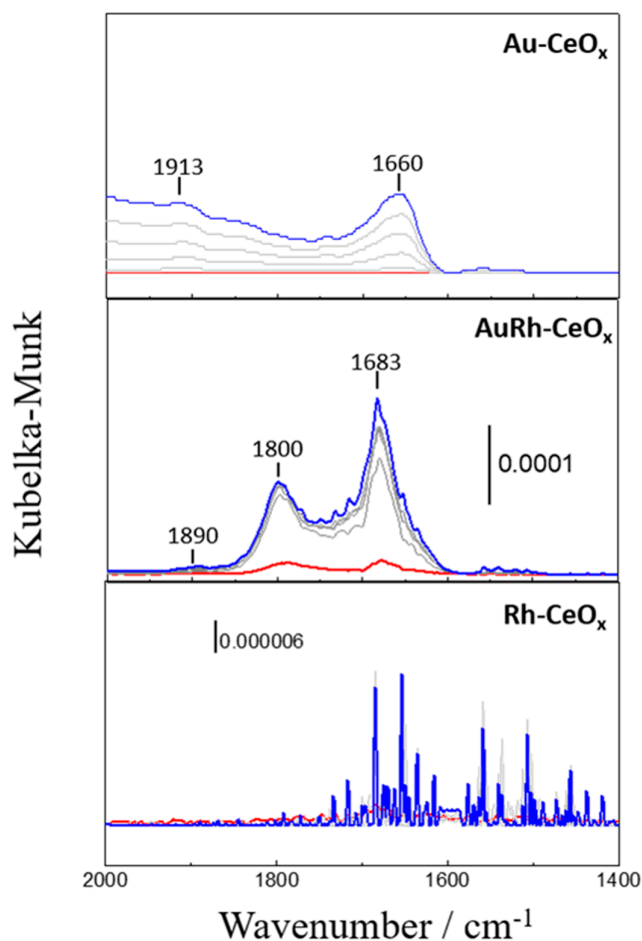
Figure 12. In situ DRIFTS spectra recorded during NO adsorption on the Au–CeO$_x$/Al$_2$O$_3$, AuRh–CeO$_x$/Al$_2$O$_3$, and Rh–CeO$_x$/Al$_2$O$_3$ catalysts at 30 °C for 5 min (from the red line to the blue line at an interval of 1 min). Gas mixture: 2000 ppm NO and He balance; total flow rate: 100 mL/min.

In situ DRIFT spectra during the reduction of NO by CO at 200 °C for 10 min are shown in Figure 13. A broad band at 1835–1842 cm^{-1} and a band at 1910 cm^{-1} were assigned to a dinitrosyl complex and positively charged Rh–NO$^+$ species, respectively [3]. The intensity of isocyanate species (-NCO) reached a maximum after 5 min for the AuRh(1:1)/Al$_2$O$_3$ catalyst, but only took 1 min for the AuRh–CeO$_x$/Al$_2$O$_3$ catalyst, showing that CeO$_x$ promoted the formation of isocyanate species. For the AuRh–CeO$_x$(1:2)/Al$_2$O$_3$ and AuRh–Ce(1:5)/Al$_2$O$_3$ catalysts with AuRh:Ce molar ratios of 1:2 and 1:5, respectively, a new band at 2173–2196 cm^{-1} assignable to isocyanate species on CeO$_x$ emerged, suggesting the spill-over of isocyanate species from bimetallic AuRh particles to the CeO$_x$ surface. Note that, for the catalysts with a large amount of CeO$_x$, the intensity of isocyanate species decreased greatly after reaching its maximum (highlighted with green and blue lines). This suggested that CeO$_x$ does not only promote the formation of isocyanate species, but also its decomposition to form N$_2$ and CO$_2$. The rapid decomposition of isocyanate species was also confirmed by switching the gas stream from NO and CO to only NO (Figure S7 in Supplementary Materials). For all the catalysts, only bands of Rh$^+$-(CO)$_2$ at 2017–2090 cm^{-1} were observed under reaction conditions. The Rh$^+$-(CO)$_2$ species seem stable and are most likely not involved in the reaction. This fact further substantiates the vital role of metallic Rh in the reaction. For the catalysts with high CeO$_x$ loadings, i.e., AuRh–CeO$_x$(1:2)/Al$_2$O$_3$ and AuRh–CeO$_x$(1:5)/Al$_2$O$_3$ catalysts, bands located in the region between 1500 and 1700 cm^{-1}, assigned to nitrate and carbonate species [3,4], grew stronger and more stable. However, the NO conversion and N$_2$ selectivity stayed almost the same for the AuRh–CeO$_x$(1:2)/Al$_2$O$_3$ and

AuRh–CeOₓ(1:5)/Al₂O₃ catalysts (Table S2 in Supplementary Materials). Therefore, these species are considered to be merely spectator species.
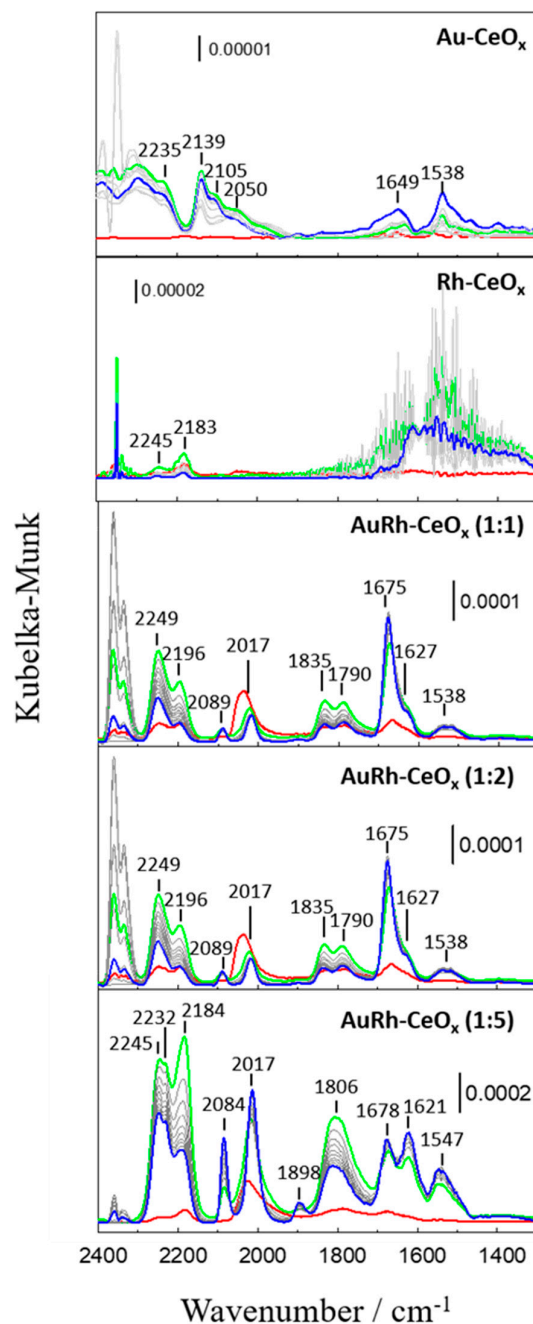

Figure 13. In situ DRIFTS spectra measured during NO–CO reaction on the Au–CeOₓ/Al₂O₃, Rh–CeOₓ/Al₂O₃, and AuRh–CeOₓ/Al₂O₃ catalysts with different molar ratios of AuRh:Ce at 200 °C for 10 min (from the red line to the blue line at an interval of 1 min). Gas mixture: 2000 ppm NO, 2000 ppm CO, and He balance; total flow rate: 100 mL/min.

3. Materials and Methods

3.1. Catalyst Preparation

A commercially available aluminum oxide (Sigma-Aldrich, nanopowder, particle size: <50 nm, St. Louis, USA) was used as a catalyst support. Chloroauric acid (HAuCl₄, Energy Chemical, 98%,

Shanghai, China), rhodium(III) chloride trihydrate (RhCl$_3$·3H$_2$O, Damas-Beta, 98%, Shanghai, China), ammonium cerium(IV) nitrate (Sigma-Aldrich, 98%, St. Louis, USA), PEG-2000 (polyethylene glycol, Energy Chemical), and sodium borohydride (NaBH$_4$, Energy Chemical, 98%, Shanghai, China) were all used without further purification.

Au, Rh, and bimetallic AuRh nanoparticles supported on Al$_2$O$_3$ were synthesized by aqueous-phase co-reduction of corresponding metal salts with NaBH$_4$ at room temperature [47]. In a typical synthetic method, 3.7 mL of deionized water, 200 mL of PEG-2000 (80 g/L), and 1 mL of 50 mM solutions of HAuCl$_4$ and RhCl$_3$·3H$_2$O were stirred together in a 50 mL glass vial for 20 min. The Au:Rh molar ratios of the metal salts were adjusted 1:0, 3:1, 1:1, 1:3, and 0:1, keeping the total metal loading at a nominal value of 3 wt.%. Al$_2$O$_3$ powder was then added to the solution under constant stirring. Afterwards, 100 mL of 20 g/L NaBH$_4$ aqueous solution were added slowly to the solution and the suspension was stirred for 1 h. The resulting particles in the suspension were then separated by centrifugation, washed several times with ethanol and dried at 60 °C overnight.

AuRh–CeO$_x$/Al$_2$O$_3$ catalysts with different molar ratios of AuRh:Ce (1:1, 2:1, and 1:5) were prepared by post-impregnation with a ceria precursor of the AuRh(1:1)/Al$_2$O$_3$ catalyst. Ammonium cerium(IV) nitrate was dissolved in 100 mL of deionized water and stirred for 30 min. The AuRh(1:1)/Al$_2$O$_3$ powder was then added to the solution and the suspension was stirred for 1 h. Afterwards, the suspension was transferred to a rotary evaporator and aged for 1 h at 60 °C, followed by the evaporation of the water at 35 °C under vacuum and drying at 60 °C overnight.

As the reference catalysts, Rh/Al$_2$O$_3$ and CeO$_x$/Al$_2$O$_3$ with a molar amount of CeO$_x$ corresponding to that in AuRh–CeO$_x$(1:1)/Al$_2$O$_3$ were synthesized in the same manner. These samples were calcined at 500 °C for 3 h before reductive pretreatment.

All catalyst samples were pretreated with pure H$_2$ at a flow rate of 100 mL/min for 1 h at 300 °C (ramping rate: 5 °C /min) prior to characterization by nitrogen adsorption, X-ray diffraction (XRD), X-ray photoelectron spectroscopy (XPS), scanning transmission electron microscopy (STEM), energy-dispersive X-ray spectroscopy (EDX), and diffuse reflectance IR spectroscopy (DRIFTS) as well as catalytic tests.

3.2. Catalyst Characterization

Brunauer-Emmett-Teller (BET) surface areas were determined from N$_2$ adsorption isotherms measured at a liquid nitrogen temperature using a Quadrasorb SI instrument (Quantachrome, Boynton Beach, FL, USA). Prior to measurements, the as-prepared samples were degassed at 150 °C for 1 h to remove residual water adsorbed on the surface and in the pores. Temperature-programmed reduction (TPR) was carried out with a Quantachrome, ChemBET Pulsar TPR/TPD (temperature-programmed desorption) instrument. One-hundred milligrams of the as-prepared (unreduced) samples were loaded in a U-shaped quartz micro-reactor and then heated at a ramping rate of 10 °C/min in 10 vol% H$_2$ in Ar at a total flow rate of 15 mL/min. TPR signals were calibrated by injecting different amounts of 10 vol% H$_2$ in Ar.

XRD measurements were carried out ex situ using a PANalytical X'Pert diffractometer (Great Malvern, UK) with Pd-filtered Cu Kα radiation at 60 kV and 55 mA. The surface compositions and oxidation states of the catalysts were analyzed by XPS on a Thermo ESCALAB 250Xi instrument using Al Kα radiation (1486.6 eV, 15 kV, and 10.8 mA) to excite photoelectrons at a 50 eV pass energy at an energy scale calibrated versus Ag 3d$_{5/2}$ at 1 eV. The instrument was equipped with an in situ pretreatment chamber connected to the XPS chamber. The sample holder was transferred between the two chambers by a manipulator. The pretreatment conditions were the same as those described in Section 3.3. STEM (JEOL, JEM-2100, 200 kV, Tokyo, Japan) was used to examine the size distribution of the mono- and bimetallic nanoparticles deposited on the alumina support and EDX was employed to gain some information about the elemental distributions of Au and Rh in the nanoparticles. The samples previously pretreated with pure hydrogen for 1 h at 300 °C were used for both STEM and EDX measurements. Particle size distributions were based on analyzing more than 100 particles per sample.

In situ IR spectroscopic studies were carried out using a Fourier-transform infrared spectrometer (Bruker Optics, Vertex 70, Billerica, MA, USA) equipped with a liquid N_2-cooled mercury cadmium telluride (MCT) detector at a spectral resolution of 4 cm^{-1} and a scanning velocity of 60 kHz. A ceramic cup with 20 mg of the samples was placed in an in situ DRIFTS reactor with three ZnSe windows, connected to an automated 4-way Valco valve (VICI AG International) and mass flow controllers (Azbil Control Solution Co., Ltd., Tokyo, Japan). The DRIFTS compartment and all the IR beam lines were purged with dry air supplied by a compressor/dryer-combined system (EKOM) to remove the H_2O vapor, of which IR bands overlapped with the IR fingerprint regions. Prior to in situ DRIFTS measurements, the catalysts were exposed to pure H_2 at a flow rate of 100 mL/min for 1 h at 300 °C (ramping rate: 5 °C /min) in the DRIFTS reactor. For all the experiments, 2000 ppm NO and/or 2000 ppm CO in He balance (He purity: 99.9999%) were utilized at a total flow rate of 100 mL/min. Before all IR measurements, background spectra were taken under helium flow.

3.3. Catalytic Reaction

The catalytic performance was examined employing a fixed-bed micro-flow reactor system. Three-hundred milligrams of catalysts were packed into the stainless-steel tube reactor with an inner diameter of 8 mm. Prior to catalytic tests, the catalysts were pretreated with pure H_2 (flow rate: 100 mL/min) at 300 °C for 1 h at a ramping rate of 5 °C/min. Residual H_2 in the gas lines and adsorbed hydrogen on the catalyst surface were removed by keeping the catalyst in a He stream at 300 °C for 10 min. Afterwards, the reactor was cooled to 50 °C and a gas mixture (2000 ppm CO and 2000 ppm NO in He balance) was added at a total flow rate of 150 mL/min, affording a gas hourly space velocity (GHSV) of 18,000 h^{-1} (length of catalyst bed: 1 cm, catalyst bed volume: 0.5 cm^3). The gaseous compositions were analyzed using a gas chromatograph (Fili, 9750 GC, Shanghai, China) equipped with a TCD detector and a molecular sieve 5A column and a NO-NO_2-NO_x analyzer (Thermo Scientific, 42i-HL, Waltham, MA, USA). Catalytic performance data were recorded after the gaseous compositions at the reactor outlet reaching a steady-state (30–70 min) at each measurement temperature. The same experiments were repeated three times to ensure the reproducibility of the data (less than ±1.0%). Blind tests using the empty tube reactor showed no significant activity.

4. Conclusions

Bimetallic AuRh nanoparticles with different Au:Rh ratios (3:1, 1:1, and 1:3) and mean sizes (3–7 nm) were prepared by aqueous-hase co-reduction of corresponding noble metal salts with $NaBH_4$ and deposited on alumina as a support. The nanoparticles were made up of well-distributed noble metal atoms forming an alloy with Rh enriched in the surface region. The AuRh/alumina catalysts were examined, concerning their potential for the reduction of NO by CO. The activity for NO reduction decreased with the increasing Au:Rh ratio, most likely due to unfavorable formation of cationic Rh clusters Rh^+-$(CO)_2$ in the presence of the reactant CO, as uncovered by in situ DRIFTS. To explore the feasibility of enhancing the performance of the bimetallic AuRh/Al_2O_3 catalysts, cerium oxide was added to the AuRh(1:1)/Al_2O_3 catalyst by post-impregnation. DRIFTS, XPS, and XRD analyses showed that Ce was present as Ce^{3+} and Ce^{4+} in the form of well-dispersed CeO_x. The catalytic performances of the AuRh–CeO_x/Al_2O_3 catalyst as well as that of the Rh/Al_2O_3 catalyst were strongly enhanced compared to that of the parent AuRh(1:1)/Al_2O_3 catalyst, contrasting the behavior of the Au–CeO_x/Al_2O_3 catalyst where ceria doping had no beneficial effect on the catalytic performance. The reason for the activity enhancement is ascribed to the redox properties of CeO_x facilitating the creation of metallic Rh sites, which are considered to be crucial for the reduction of NO by CO. Furthermore, in situ DRIFTS investigations during the reduction of NO by CO at 200 °C proved that the presence of CeO_x enhances the formation of intermediate isocyanate species and their reaction with NO to produce N_2 and CO_2. Finally, it should be stressed that it might be possible to further enhance the catalytic performance the AuRh–CeO_x/Al_2O_3 catalyst for the reduction of NO by CO by optimizing their composition. Overall, the study shows that alumina-supported bimetallic AuRh catalysts hardly provide a better catalytic performance in the reduction of NO by CO,

compared to the well-known monometallic Rh/alumina catalyst. Doping with ceria enhances the catalytic performance of both catalysts.

References

1. Taylor, K.A.; Paskewitz, S.M.; Copeland, R.S.; Koros, J.; Beach, R.F.; Githure, J.I.; Collins, F.H. Comparison of two ribosomal DNA-based methods for differentiating members of the Anopheles gambiae complex (Diptera: Culicidae). *J. Med. Entomol.* **1993**, *30*, 457–461.

2. Shelef, M.; Graham, G.W. Why Rhodium in Automotive Three-Way Catalysts? *Catal. Rev.* **1994**, *36*, 433–457.

3. Chafik, T.; Kondarides, D.I.; Verykios, X.E. Catalytic Reduction of NO by CO over Rhodium Catalysts. *J. Catal.* **2000**, *190*, 446–459.

4. Kondarides, D.I.; Chafik, T.; Verykios, X.E. Catalytic Reduction of NO by CO over Rhodium Catalysts. *J. Catal.* **2000**, *193*, 303–307.

5. Kondarides, D.I.; Chafik, T.; Verykios, X.E. Catalytic Reduction of NO by CO over Rhodium Catalysts: 2. Effect of Oxygen on the Nature, Population, and Reactivity of Surface Species Formed under Reaction Conditions. *J. Catal.* **2000**, *191*, 147–164.

6. Honkala, K.; Pirilä, P.; Laasonen, K. CO and NO adsorption and co-adsorption on the Pd(1 1 1) surface. *Surf. Sci.* **2001**, *489*, 72–82.

7. Khristova, M.S.; Petrović, S.P.; Terlecki-Baričević, A.; Mehandjiev, D.R. Catalytic reduction of NO by CO over Pd—Doped Perovskite-type catalysts. *Cent. Eur. J. Chem.* **2009**, *7*, 857.

8. Rasko, J.; Szabo, Z.; Bansagi, T.; Solymosi, F. FTIR study of the photo-induced reaction of NO + CO on Rh/TiO$_2$. *Phys. Chem. Chem. Phys.* **2001**, *3*, 4437–4443.

9. Ivanova, E.; Mihaylov, M.; Thibault-Starzyk, F.; Daturi, M.; Hadjiivanov, K. FTIR spectroscopy study of CO and NO adsorption and co-adsorption on Pt/TiO$_2$. *J. Mol. Catal. A Chem.* **2007**, *274*, 179–184.

10. Haruta, M.; Kobayashi, T.; Sano, H.; Yamada, N. Novel gold catalysts for the oxidation of carbon monoxide at a temperature far below 0 °C. *Chem. Lett.* **1987**, *16*, 405–408.

11. Ayati, A.; Ahmadpour, A.; Bamoharram, F.F.; Tanhaei, B.; Mänttäri, M.; Sillanpää, M. A review on

catalytic applications of Au/TiO2 nanoparticles in the removal of water pollutant. *Chemosphere* **2014**, *107*, 163–174.

12. Corti, C.W.; Holliday, R.J.; Thompson, D.T. Commercial aspects of gold catalysis. *Appl. Catal. A-Gen.* **2005**, *291*, 253–261.

13. Sugunan, A.; Thanachayanont, C.; Dutta, J.; Hilborn, J.G. Heavy-metal ion sensors using chitosan-capped gold nanoparticles. *Sci. Technol. Adv. Mater.* **2005**, *6*, 335.

14. Daniel, M.-C.; Astruc, D. Gold Nanoparticles: Assembly, Supramolecular Chemistry, Quantum-Size-Related Properties, and Applications toward Biology, Catalysis, and Nanotechnology. *Chem. Rev.* **2004**, *104*, 293–346.

15. Ishida, T.; Haruta, M. Gold catalysts: Towards sustainable chemistry. *Angew. Chem. Int. Ed.* **2007**, *46*, 7154–7156.

16. Haruta, M. Novel catalysis of gold deposited on metal oxides. *Catal. Surv. Asia* **1997**, *1*, 61–73.

17. Hashmi, A.S.K.; Hutchings, G.J. Gold catalysis. *Angew. Chem.-Int. Ed.* **2006**, *45*, 7896–7936.

18. Mallat, T.; Baiker, A. Potential of Gold Nanoparticles for Oxidation in Fine Chemical Synthesis. *Annu. Rev. Chem. Biomol. Eng.* **2012**, *3*, 11–28.

19. Min, B.K.; Friend, C.M. Heterogeneous gold-based catalysis for green chemistry: Low-temperature CO oxidation and propene oxidation. *Chem. Rev.* **2007**, *107*, 2709–2724.

20. Stratakis, M.; Garcia, H. Catalysis by Supported Gold Nanoparticles: Beyond Aerobic Oxidative Processes. *Chem. Rev.* **2012**, *112*, 4469–4506.

21. Ilieva, L.; Pantaleo, G.; Velinov, N.; Tabakova, T.; Petrova, P.; Ivanov, I.; Avdeev, G.; Paneva, D.; Venezia, A.M. NO reduction by CO over gold catalysts supported on Fe-loaded ceria. *Appl. Catal. B-Environ.* **2015**, *174*, 176–184.

22. Bond, G.C.; Thompson, D.T. Catalysis by Gold. *Catal. Rev.* **1999**, *41*, 319–388.

23. Debeila, M.A.; Coville, N.J.; Scurrell, M.S.; Hearne, G.R. DRIFTS studies of the interaction of nitric oxide and carbon monoxide on Au–TiO2. *Catal. Today* **2002**, *72*, 79–87.

24. Ueda, A.; Haruta, M. Nitric oxide reduction with hydrogen, carbon monoxide, and hydrocarbons over gold catalysts. *Gold Bull.* **1999**, *32*, 3–11.

25. Gao, F.; Wang, Y.; Goodman, D.W. CO/NO and CO/NO/O2 reactions over a Au–Pd single crystal catalyst. *J. Catal.* **2009**, *268*, 115–121.

26. Granger, P.; Dujardin, C.; Paul, J.F.; Leclercq, G. An overview of kinetic and spectroscopic investigations on three-way catalysts: Mechanistic aspects of the CO + NO and CO + N2O reactions. *J. Mol. Catal. A Chem.* **2005**, *228*, 241–253.

27. da Cunha, M.C.P.M.; Weber, M.; Nart, F.C. On the adsorption and reduction of NO3- ions at Au and Pt electrodes studied by in situ FTIR spectroscopy. *J. Electroanal. Chem.* **1996**, *414*, 163–170.

28. Venkov, T.; Fajerwerg, K.; Delannoy, L.; Klimev, H.; Hadjiivanov, K.; Louis, C. Effect of the activation temperature on the state of gold supported on titania: An FT-IR spectroscopic study. *Appl. Catal. A-Gen.* **2006**, *301*, 106–114.

29. Klimev, H.; Fajerwerg, K.; Chakarova, K.; Delannoy, L.; Louis, C.; Hadjiivanov, K. Oxidation of gold metal particles supported on TiO2: An FTIR study by means of low-temperature CO adsorption. *J. Mater. Sci.* **2007**, *42*, 3299–3306.

30. Solymosi, F.; Bánsági, T.; Suli Zakar, T. Surface interaction and reaction of NO + CO on a supported Au catalyst. *Phys. Chem. Chem. Phys.* **2003**, *5*, 4724–4730.

31. Solymosi, F.; Bánsági, T.; Zakar, T.S. Infrared Study of the NO + CO Interaction over Au/TiO2 Catalyst.

Catal. Lett. **2003**, *87*, 7–10.

32. Fernández-García, M.; Gómez Rebollo, E.; Guerrero Ruiz, A.; Conesa, J.C.; Soria, J. Influence of ceria on the dispersion and reduction/oxidation behaviour of alumina-supported copper catalysts. *J. Catal.* **1997**, *172*, 146–159.

33. Martínez-Arias, A.; Fernández-García, M.; Hungría, A.B.; Iglesias-Juez, A.; Duncan, K.; Smith, R.; Anderson, J.A.; Conesa, J.C.; Soria, J. Effect of thermal sintering on light-off performance of Pd/(Ce,Zr)O$_x$/Al$_2$O$_3$ three-way catalysts: Model gas and engine tests. *J. Catal.* **2001**, *204*, 238–248.

34. Ge, C.; Liu, L.; Liu, Z.; Yao, X.; Cao, Y.; Tang, C.; Gao, F.; Dong, L. Improving the dispersion of CeO$_2$ on γ-Al$_2$O$_3$ to enhance the catalytic performances of CuO/CeO$_2$/γ-Al$_2$O$_3$ catalysts for NO removal by CO. *Catal. Commun.* **2014**, *51*, 95–99.

35. Trovarelli, A. Catalytic Properties of Ceria and CeO$_2$-Containing Materials. *Catal. Rev.* **1996**, *38*, 439–520.

36. Cunningham, J.; O'Brien, S.; Sanz, J.; Rojo, J.M.; Soria, J.A.; Fierro, J.L.G. Exceptional susceptibility of ceria-supported rhodium catalyst to inhibitory SMSI effects including acetone hydrogenation. *J. Mol. Catal.* **1990**, *57*, 379–396.

37. Liu, N.; Chen, X.; Zhang, J.; Schwank, J.W. DRIFTS study of photo-assisted catalytic CO + NO redox reaction over CuO/CeO$_2$-TiO$_2$. *Catal. Today* **2015**, *258 Pt 1*, 139–147.

38. Chen, J.; Zhan, Y.; Zhu, J.; Chen, C.; Lin, X.; Zheng, Q. The synergetic mechanism between copper species and ceria in NO abatement over Cu/CeO$_2$ catalysts. *Appl. Catal. A-Gen.* **2010**, *377*, 121–127.

39. Martínez-Arias, A.; Soria, J.; Conesa, J.C.; Seoane, X.L.; Arcoya, A.; Cataluña, R. NO reaction at surface oxygen vacancies generated in cerium oxide. *J. Chem. Soc. Faraday Trans.* **1995**, *91*, 1679–1687.

40. Louis, C. Chemical Preparation of Supported Bimetallic Catalysts. Gold-Based Bimetallic, a Case Study. *Catalysts* **2016**, *6*, 110.

41. Gao, F.; Goodman, D.W. Pd-Au bimetallic catalysts: Understanding alloy effects from planar models and (supported) nanoparticles. *Chem. Soc. Rev.* **2012**, *41*, 8009–8020.

42. Duan, T.; Zhang, R.G.; Ling, L.X.; Wang, B.J. Insights into the Effect of Pt Atomic Ensemble on HCOOH Oxidation over Pt-Decorated Au Bimetallic Catalyst To Maximize Pt Utilization. *J. Phys. Chem. C* **2016**, *120*, 2234–2246.

43. Xu, C.L.; Du, Y.Q.; Li, C.; Yang, J.; Yang, G. Insight into effect of acid/base nature of supports on selectivity of glycerol oxidation over supported Au-Pt bimetallic catalysts. *Appl. Catal. B-Environ.* **2015**, *164*, 334–343.

44. Sterchele, S.; Biasi, P.; Centomo, P.; Campestrini, S.; Shchukarev, A.; Rautio, A.R.; Mikkola, J.P.; Salmi, T.; Zecca, M. The effect of the metal precursor-reduction with hydrogen on a library of bimetallic Pd-Au and Pd-Pt catalysts for the direct synthesis of H$_2$O$_2$. *Catal. Today* **2015**, *248*, 40–47.

45. Liu, L.C.; Zi, X.H.; Dai, H.X.; Zhao, Z.; Wang, X.P.; He, H. Preparation and Characterization of Rh-Au/gamma-Al$_2$O$_3$ Three-Way Nanocatalysts. *Chin. J. Catal.* **2010**, *31*, 781–787.

46. Garcia, S.; Zhang, L.; Piburn, G.W.; Henkelman, G.; Humphrey, S.M. Microwave Synthesis of Classically Immiscible Rhodium-Silver and Rhodium-Gold Alloy Nanoparticles: Highly Active Hydrogenation Catalysts. *ACS Nano* **2014**, *8*, 11512–11521.

47. Essinger-Hileman, E.R.; DeCicco, D.; Bondi, J.F.; Schaak, R.E. Aqueous room-temperature synthesis of Au-Rh, Au-Pt, Pt-Rh, and Pd-Rh alloy nanoparticles: Fully tunable compositions within the miscibility gaps. *J. Mater. Chem.* **2011**, *21*, 11599–11604.

48. Thanh-Son, N.; Laurenti, D.; Afanasiev, P.; Konuspayeva, Z.; Piccolo, L. Titania-Supported gold-based nanoparticles efficiently catalyze the hydrodeoxygenation of guaiacol. *J. Catal.* **2016**, *344*, 136–140.

49. Konuspayeva, Z.; Afanasiev, P.; Nguyen, T.-S.; Di Felice, L.; Morfin, F.; Nhat-Tai, N.; Nelayah, J.; Ricolleau, C.; Li, Z.Y.; Yuan, J.; et al. Au-Rh and Au-Pd nanocatalysts supported on rutile titania nanorods: Structure and chemical stability. *Phys. Chem. Chem. Phys.* **2015**, *17*, 28112–28120.

50. Okamoto, H.; Massalski, T.B. The Au-Rh (Gold-Rhodium) System. *Bull. Alloy. Phase Diagr.* **1984**, *5*, 384–387.

51. Piccolo, L.; Li, Z.Y.; Demiroglu, I.; Moyon, F.; Konuspayeva, Z.; Berhault, G.; Afanasiev, P.; Lefebvre, W.; Yuan, J.; Johnston, R.L. Understanding and controlling the structure and segregation behaviour of AuRh nanocatalysts. *Sci. Rep.* **2016**, *6*, 35226.

52. Monev, M.; Pfund, A.; Beck, G.; Petrov, K.; Bretzler, R.; Heuberger, U.; Zielonka, A. Effect of current density on composition and structure of electrodeposited Au–Ni alloy coatings. *Trans. IMF* **2013**, *91*, 176–181.

53. Wang, Z.-J.; Zhao, Y.; Cui, L.; Du, H.; Yao, P.; Liu, C.-J. CO_2 reforming of methane over argon plasma reduced Rh/Al_2O_3 catalyst: A case study of alternative catalyst reduction via non-hydrogen plasmas. *Green Chem.* **2007**, *9*, 554–559.

54. Zhang, H.; Deng, X.; Jiao, C.; Lu, L.; Zhang, S. Preparation and catalytic activities for H_2O_2 decomposition of Rh/Au bimetallic nanoparticles. *Mater. Res. Bull.* **2016**, *79*, 29–35.

55. Marx, S.; Krumeich, F.; Baiker, A. Surface Properties of Supported, Colloid-Derived Gold/Palladium Mono- and Bimetallic Nanoparticles. *J. Phys. Chem. C* **2011**, *115*, 8195–8205.

56. Dick, K.; Dhanasekaran, T.; Zhang, Z.Y.; Meisel, D. Size-Dependent melting of silica-encapsulated gold nanoparticles. *J. Am. Chem. Soc.* **2002**, *124*, 2312–2317.

57. Yasuda, H.; Mori, H. Cluster-Size dependence of alloying behavior in gold clusters. *Z. Phys. D At. Mol. Clust.* **1994**, *31*, 131–134.

58. Kohiki, S.; Oki, K.; Konishi, F. Extra-Atomic Relaxation Effect on the Binding Energy of Reference Gold in X-Ray Photoelectron Spectroscopy. *Anal. Sci.* **1985**, *1*, 115–117.

59. Raskó, J.; Koós, Á.; Baán, K.; Kiss, J. Characterization of $Au-Rh/TiO_2$ catalysts by CO adsorption; XPS, FTIR and TPD experiments. *React. Kinet. Catal. Lett.* **2007**, *90*, 187–195.

60. Chen, L.; Choong, C.K.S.; Zhong, Z.; Huang, L.; Ang, T.P.; Hong, L.; Lin, J. Carbon monoxide-free hydrogen production via low-temperature steam reforming of ethanol over iron-promoted Rh catalyst. *J. Catal.* **2010**, *276*, 197–200.

61. Araya, P.; Weissmann, C. FTIR study of the oxidation reaction of CO with O_2 over bimetallic $Pd–Rh/SiO_2$ catalysts in an oxidized state. *Catal. Lett.* **2000**, *68*, 33–39.

62. Evans, J.; Dent, A.J.; Diaz-Moreno, S.; Fiddy, S.G.; Jyoti, B.; Newton, M.A.; Tromp, M. *In Situ Structure-Function Studies of Oxide Supported Rhodium Catalysts by Combined Energy Dispersive XAFS and DRIFTS Spectroscopies*; X-Ray Absorption Fine Structure-Xafs13; Hedman, B., Painetta, P., Eds.; AIP: Melville, NY, USA, 2007; p. 603.

63. Iordan, A.; Zaki, M.I.; Kappenstein, C.; Geron, C. XPS and in situ IR spectroscopic studies of $CO/Rh/Al_2O_3$ and $CO/Rh/K-Al_2O_3$ at high temperatures: Probing the impact of the potassium functionalization of the support. *Phys. Chem. Chem. Phys.* **2003**, *5*, 1708–1715.

64. Gómez-Cortés, A.; Díaz, G.; Zanella, R.; Ramírez, H.; Santiago, P.; Saniger, J.M. $Au-Ir/TiO_2$ prepared by deposition precipitation with urea: Improved activity and stability in CO oxidation. *J. Phys. Chem. C* **2009**, *113*, 9710–9720.

65. Hasegawa, Y.; Haneda, M.; Kintaichi, Y.; Hamada, H. Zn-promoted Rh/SiO_2 catalyst for the selective reduction of NO with H_2 in the presence of O_2 and SO_2. *Appl. Catal. B-Environ.* **2005**, *60*, 41–47.

66. Debeila, M.A.; Coville, N.J.; Scurrell, M.S.; Hearne, G.R. Direct observation of thermally activated NO adsorbate species on Au-TiO$_2$: DRIFTS studies. *J. Mol. Catal. A Chem.* **2004**, *219*, 131–141.

67. Sobczak, I.; Musialska, K.; Pawlowski, H.; Ziolek, M. NO and C$_3$H$_6$ adsorption and coadsorption in oxygen excess—A comparative study of different type zeolites modified with gold. *Catal. Today* **2011**, *176*, 393–398.

68. Araya, P.; Gracia, F.; Cortés, J.; Wolf, E.E. FTIR study of the reduction reaction of NO by CO over Rh/SiO$_2$ catalysts with different crystallite size. *Appl. Catal. B-Environ.* **2002**, *38*, 77–90.

69. Na-Ranong, D.; Yuangsawad, R.; Kitchaiya, P.; Aida, T. Application of periodic operation to kinetic study of NO-CO reaction over Rh/Al$_2$O$_3$. *Chem. Eng. J.* **2009**, *146*, 275–286.

70. Zhu, W.; Xiao, S.; Zhang, D.; Liu, P.; Zhou, H.; Dai, W.; Liu, F.; Li, H. Highly Efficient and Stable Au/CeO$_2$–TiO$_2$ Photocatalyst for Nitric Oxide Abatement: Potential Application in Flue Gas Treatment. *Langmuir* **2015**, *31*, 10822–10830.

71. Bêche, E.; Charvin, P.; Perarnau, D.; Abanades, S.; Flamant, G. Ce 3d XPS investigation of cerium oxides and mixed cerium oxide (Ce$_x$Ti$_y$O$_z$). *Surf. Interface Anal.* **2008**, *40*, 264–267.

72. Hirano, T.; Ozawa, Y.; Sekido, T.; Ogino, T.; Miyao, T.; Naito, S. The role of additives in the catalytic reduction of NO by CO over Pd-In/SiO$_2$ and Pd-Pb/SiO$_2$ catalysts. *Appl. Catal. A-Gen.* **2007**, *320*, 91–97.

73. Hirano, T.; Ozawa, Y.; Sekido, T.; Ogino, T.; Miyao, T.; Naito, S. Marked effect of In, Pb and Ce addition upon the reduction of NO by CO over SiO$_2$ supported Pd catalysts. *Catal. Commun.* **2007**, *8*, 1249–1254.

74. Wang, X.; Maeda, N.; Baiker, A. Synergistic Effects of Au and FeO$_x$ Nanocomposites in Catalytic NO Reduction with CO. *ACS Catal.* **2016**, *6*, 7898–7906.